Elastic metamaterial-based seismic shield for both Lamb and surface waves

Qiujiao Du, Yi Zeng, Guoliang Huang, and Hongwu Yang

Citation: AIP Advances **7**, 075015 (2017); doi: 10.1063/1.4996716
View online: http://dx.doi.org/10.1063/1.4996716
View Table of Contents: http://aip.scitation.org/toc/adv/7/7
Published by the American Institute of Physics

Elastic metamaterial-based seismic shield for both Lamb and surface waves

Qiujiao Du,[1,2,a] Yi Zeng,[1] Guoliang Huang,[2] and Hongwu Yang[3]
[1]*School of Mathematics and Physics, China University of Geosciences, Wuhan 430074, China*
[2]*Department of Mechanical & Aerospace Engineering, University of Missouri, Columbia, MO 65211, USA*
[3]*School of Civil Engineering and Mechanics, Huazhong University of Science and Technology, Wuhan 430074, China*

(Received 1 February 2017; accepted 18 July 2017; published online 26 July 2017)

Controlling the propagation of seismic waves to protect critical infrastructure via metamaterial is of new topical interest. This approach can be implemented by remote shielding of incoming waves rather than with vibration isolating structures. In this paper, a two-dimensional elastic metamaterial with periodically square concrete-filled steel piles embedded in soil is proposed to achieve a seismic shield for guided Lamb waves and surface waves. Its properties are numerically investigated using the finite element method. For Lamb waves, we first identify complete bandgaps appearing in a periodic composite with cylindrical piles. By comparison, it is found that if the shape of the pile is replaced with the square shape, the bandgaps become wider and shift to the lower frequencies, which is more suitable for practical applications. Furthermore, it is demonstrated that a complete low frequency bandgap also exists for surface waves. The vibration modes for both types of waves at the bandgap edges are computed and analyzed to clarify the mechanism of the bandgap generation. The study focuses on realistic structures that can be effective in the frequency ranges for seismic waves. Although we have focused on the geophysical setting, elastic waves are also very important in applications involving acoustic wave devices. [http://dx.doi.org/10.1063/1.4996716]

I. INTRODUCTION

Catastrophic damage to humans during earthquakes is mainly caused by the collapse of buildings. Methods to reinforce buildings to withstand earthquakes have been an urgent concern for architects and researchers. The conventional engineering methods are dampers, wave scatters and rubbers to protect the buildings from damage by swaying or vibration. These methods are based on reinforcing buildings using additional passive energy dissipation systems integrated in the framing structure of a building. Although they are generally effective, they cannot be flexibly adapted to structural changes,[1,2] and have high costs. In addition, they are inefficient for large earthquakes. However, recently developed earthquake engineered metamaterials open a new way to counterattack seismic waves. The metamaterial actively controls the seismic waves by providing an additional shield around the protected building rather than reconstructing the building structure. Compared with common engineering solutions, as previous mentioned, the advantage of the metamaterial method is that it can not only attenuate seismic waves before they reach critical targets, but also protect a distributed area rather than an individual building.

Metamaterials first appeared seventeen years ago[3] and quickly formed a major research area owing to their capabilities to manipulate the propagation of waves with novel properties which

[a]Email: qiujiaodu@cug.edu.cn

natural materials do not have.[4] Although originating from electromagnetism, the field of metamaterial research has rapidly expanded to novel applications in acoustics and elasticity. Locally resonant sonic metamaterials composed of three dimensional cubic arrays of thin coated spheres[5] and fluid-filled Helmholtz resonators[6] opened the way for elastic and acoustic analogues of electromagnetic metamaterials.[7] Frequency filtering,[8] invisibility[9,10] and super-resolution imaging[11] of acoustic metamaterials have been demonstrated. In recent years, Guenneau et al. successively researched metamaterials controlling elastic waves in thin plates numerically[12,13] and experimentally,[14] which inspired them to cooperate with civil engineers in the Ménard company to control surface seismic waves by exploring metamaterials with potential applications in mitigating the destructive effects of earthquakes.[15] Their experimental results demonstrated that an artificial structure built around a target can deflect incoming acoustic waves at a frequency relevant to earthquake protection, and the experimental results agreed well with simulations. The preliminary success of this seismic field test proves the feasibility of analogies with control of electromagnetic and acoustic waves.

Then, some researchers have explored the intriguing domain of application in anti-earthquake devices although the challenges are substantial because seismic waves are more complex than electromagnetic and acoustic waves. Presently, there are two main ideas to control the propagation of seismic waves. One is a cloaking method and the other is a crystal method. Cloaking has a general property that steers the wave propagation around the protected target due to the gradual effective refractive index.[12,13] The crystal method utilizes its fundamental property of bandgap formation where elastic waves are reflected or trapped regardless of incident angle and polarization.[16] For the cloaking method, the seismic waves bend around the foundation of the protected building by matching impedances when they pass through the metamaterial layers instead of reflecting or attenuating seismic waves. Thus, the seismic waves would still destroy the surrounding buildings. In contrast, the seismic crystal would create an artificial shadow zone by producing the imaginary velocity of the wave in the bandgaps. Some of the energy carried by the seismic waves is transformed into another type of energy, such as sound and heat. Thus, the crystal protects not only the protected building but also the surrounding buildings. The current research interest mainly focuses on the latter method.

Recently, a metamaterial-based seismic shield with a two-dimensional (2D) periodic system of pile barriers was reported and strong decay within the bandgaps was demonstrated numerically.[17] Periodic arrangements of boreholes demonstrated attenuation behaviors in the Bragg scattering regime for anti-earthquake applications in large-scale experiments.[15] Locally resonant structures have been shown to give rise to so-called super-wide pseudo-directional bandgaps in elastic crystals.[18] More recently, resonant sub-wavelength scatterers on an elastic substrate have been investigated and showed that natural forest trees can effectively weaken the seismic waves in the bandgaps created by local resonances between trees and elastic waves in the substrate.[19] Colquitt et al. provided the theoretical and analytical framework for a seismic metamaterial with an array of resonators by studying two canonical problems associated with the control of mechanical surface waves.[20]

In previous seismic metamaterial research, the surface waves are usually of primary interest. However, guided Lamb waves, originally misinterpreted as Rayleigh waves, are ignored. In fact, Lamb waves can be generated in near-surface seismic events,[21] when for instance the soil is in the horizontal fracture within a consolidated rock where the stiffness virtually vanishes, or is bounded by a deep layer filled with gas. Guided Lamb waves can carry seismic energy and propagate long distances, and usually dominate in the seismic records of local and regional events.[22] Guided Lamb waves may play a key role in the earthquake response of buildings and should be accounted for in the design of real seismic shields.

In this paper, we achieve a broadband seismic metamaterial by introducing resonant structures at the sites of a square lattice. Bandgap characteristics of Lamb and surface waves in the periodic structures are calculated and the wave propagation along the plane perpendicular to the piles is investigated using the finite element method (FEM). The periodic piles are usually regarded as a 2D periodic composite analogously, but surface wave propagation in the periodic composite is indeed a three-dimensional (3D) problem. In particular, 2D models may overestimate the bandgap width in the case of locally resonant metamaterials because the out-of-plane mode is ignored. Therefore, here we study the bandgap using a 3D model. To foster experimental efforts, we provide a

simplified structure using no more than two different materials which are common building materials. This metamaterial is suitable for potential application in passive anti-earthquake systems for smart buildings.

II. MODEL AND METHOD

In our work, seismic waves can be characterized as elastic waves propagating through the inhomogeneous ground. Suppose the seismic surface waves propagate along the periodic plane (i.e., the x-y plane) and the z-axis is along the height direction. The governing equations describing the time-harmonic motions in inhomogeneous materials can be expressed by

$$\nabla \cdot (\mathbf{C}(\mathbf{r}) : \nabla \mathbf{u}(\mathbf{r})) = -\rho(\mathbf{r})\omega^2 \mathbf{u}(\mathbf{r}) \tag{1}$$

where $\mathbf{C}$ is the fourth-order elasticity tensor, $\mathbf{r}$ denotes the position vector, $\mathbf{u}$ is the displacement vector, ω is the angular frequency and ρ is the mass density of constituent material.

In order to demonstrate the band structures and the wave attenuation effect of the proposed structures, we apply FEM which is a common numerical analysis technique used in elastic wave simulations.[23,24] Compared with other traditional methods, such as the plane wave expansion method,[25] the finite difference time domain method,[26] the wavelet method,[27] the multiple-scattering method[28] and the boundary element method,[29] FEM has merits such as its compatibility, good convergence, high accuracy and efficiency. The characteristics of wave propagation in periodic composites can be captured by calculating the representative volume unit cell based on Floquet-Bloch theory. The unit cell is meshed according to the variation of the structures and divided into finite elements connected by nodes. The discrete form of the eigenvalue equations at the nodes in the unit cell can be written as

$$(\mathbf{K} - \omega^2 \mathbf{M})\mathbf{u} = 0 \tag{2}$$

where $\mathbf{u}$ is the displacements at the nodes, $\mathbf{K}$ and $\mathbf{M}$ are the global stiffness and mass matrices of the unit cell, respectively.

In the calculation, Floquet periodic boundary conditions are applied along the x- and y-axis directions of the volume such that[30–34]

$$\mathbf{u}(\mathbf{r} + \mathbf{R}) = \mathrm{e}^{\mathrm{i}\mathbf{k}\cdot\mathbf{R}}\mathbf{u}(\mathbf{r}) \tag{3}$$

where $\mathbf{r}$ is the location vector, $\mathbf{R}$ is the lattice translation vector and $\mathbf{k}$ is the wave vector.

Traction free conditions are applied to the top and bottom surfaces of the unit cell to model Lamb waves, that is, the traction components on the surfaces are zero. For surface waves, a semi-infinite medium is considered. An approach is adopted by adding a very thick substrate to the pile structure to decouple the Lamb waves into two surface waves in each surface of the thick unit cell. Specific boundary conditions are applied and a sound cone is introduced.[35–40] Then, COMSOL is utilized to directly solve the eigenvalue problem given by Eq. (2) under the complex boundary condition. The wave vector $\boldsymbol{k}$ sweeps the edges of the irreducible Brillouin zone, so that the total dispersion relations are obtained.

The proposed metamaterials with different unit cells are designed, as shown in Fig. 1, and each metamaterial consists of a periodic array of piles embedded in the soil with a square lattice. The schematic diagrams of the corresponding unit cells are given and the corresponding geometric parameters are also labeled in Fig. 1. The distance between the centers of the scatterers (steel piles) is referred as the lattice constant and denoted as a. The parameter h is the height of the piles and the outer and inner radii of the cylindrical scatterers are denoted by R and r, respectively. The length and width of the outer side of the hollow rectangle steel piles are denoted by d_1 and e_1, respectively, and the length and width of the inner side are denoted by d_2 and e_2. The outer side-length and inner side-length of the hollow square steel piles are represented by b and c, respectively. The volume fraction of the steel part in the hollow cylinder unit cell is same as that in the hollow rectangle pile unit cell and square pile unit cell, as shown in Fig. 1(a), (b) and (c). The structure in Fig. 1(d) is constructed by filling concrete or soil into the hollow steel pile in Fig.(c).

Due to the velocity of seismic surface waves in superficial and under consolidated material from less than $100\mathrm{ms}^{-1}$ to $300\mathrm{ms}^{-1}$, the wavelength of surface waves induced by natural seismic sources are

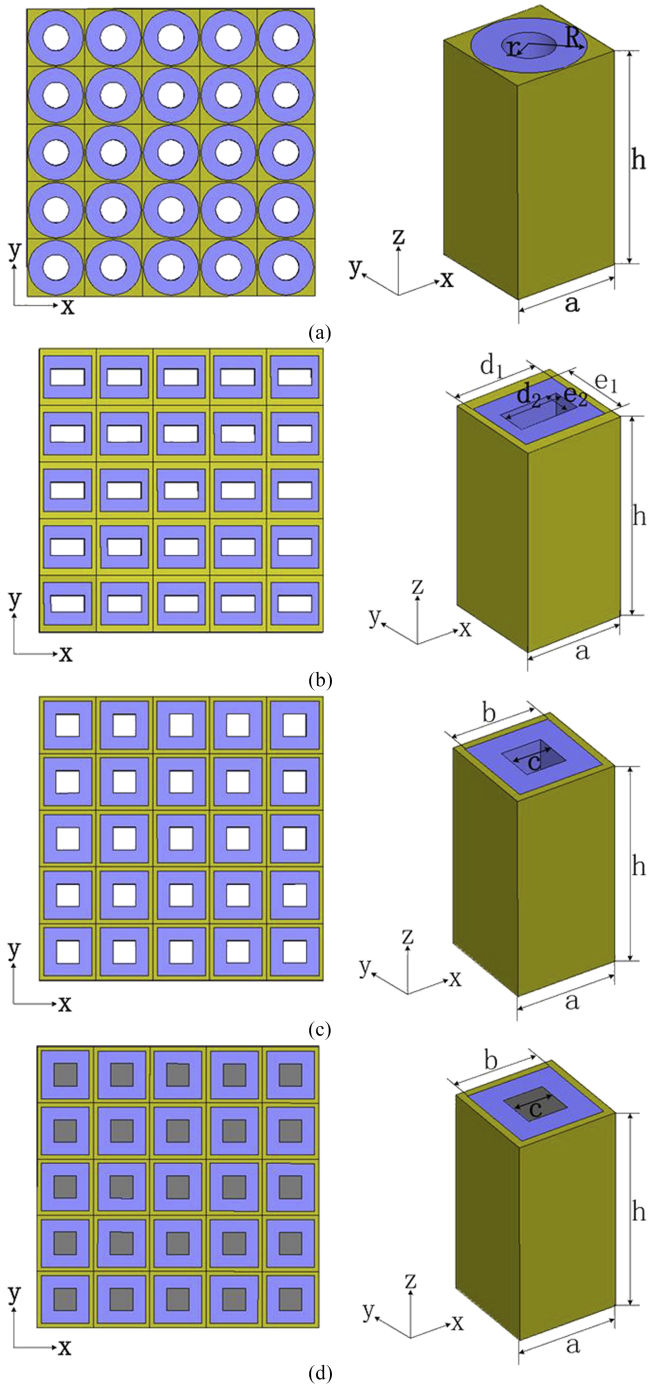

FIG. 1. Schematic illustration of the seismic metamaterial structure arrays and corresponding unit cells with the square lattice constant a = 10m and the height h = 20m: (a) hollow cylinder with geometric parameters: $R = 0.48a$, $r = 0.23a$; (b) hollow rectangle pile with geometric parameters: d_1=0.9a, e_1=0.8a, d_2=0.63a, e_2=0.25a; (c) hollow square pile with geometric parameters: $b = 0.85a$, $c = 0.4a$; (d) concrete-filled (or soil-filled) pile with the same geometric parameters as (c). The yellow, blue and grey areas represent soil, steel and concrete, respectively.

of the order of 100m. Therefore, we consider the lattice constant of a = 10m. Equation (2) is solved by imposing two components of the wave vector and the band structures are obtained by scanning of the wave vectors in the first irreducible Brillouin zone (FIBZ). The FIBZ is constructed by calculating the associated reciprocal lattices of the periodic composites and its shape is illustrated in Fig. 2.

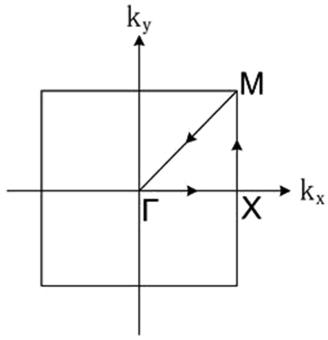

FIG. 2. The first irreducible Brillouin zone for the periodic composites with square lattice: $M = (\pi/a,\pi/a)$, $\Gamma = (0,0)$, $X = (\pi/a,0)$.

Considering practical applications, we choose soil as a host medium and the common building materials as the composite materials, such as steel and concrete. In our work, we assume the materials are linear elastic, homogeneous and isotropic. The corresponding material parameters of soil are followed as: Young's modulus of soil E_s=30MPa, Poisson's ratio μ_s=0.3 and mass density ρ_s=1800kg/m^3. The parameters of steel are: Young's modulus E_{st}=210GPa, Poisson's ratio μ_{st}=0.3 and mass density ρ_{st}=7850kg/m^3. The parameters of concrete are: Young's modulus E_c=40GPa, Poisson's ratio μ_c=0.2 and mass density ρ_c=2500kg/m^3.

III. DISCUSSION

A. Band structures for Lamb waves

Seismic waves arise from the superposition of different bulk and surface waves as a result of complex subterranean formation. For example, Lamb waves can be generated during the near-surface seismic surveys whenever there is a layer at the depth whose shear-wave velocity is significantly smaller than that of the overlaying layer. To begin with, numerical simulations are performed to predict the bandgap properties for Lamb waves. We select hollow steel piles with three kinds of common shapes, namely, circular, rectangle and square cross-sections, to investigate the effect of geometric shape on the evolution of bandgaps. For comparison purposes, the height of the unit cell and the volume fraction of steel for the three types are both set as 20m and 0.56. Figure 3 (a), (b) and (c) show the band structures of periodic composites with three different cross-sectional shapes, respectively. First, six complete bandgaps (CBGs) are found in the frequency range considered with hollow cylinder structures shown in Fig. 3(a). The first CBG with a width of 2.7Hz is obtained between 9.32Hz and 12.02Hz, and is produced between the sixth and seventh bands. The second CBG with a width of 1.35Hz is obtained between 12.40Hz and 13.75Hz, and is produced between the eighth and ninth bands. The third CBG with a width of 2.66Hz is obtained between 13.75Hz and 16.41Hz, and is produced between the ninth and tenth bands. One may also notice that the second and third CBGs are connected because the ninth band is flat. In addition, the widths of the fourth, fifth and sixth CBGs are 0.59Hz, 0.86Hz and 0.62Hz, respectively. Second, for hollow rectangle pile structures, CBG with a width of 10.57Hz between 9.16Hz and 19.73Hz is obtained, which is produced between the sixth and seventh bands. In Fig. 3(b), the upper band edge of the CBG increases, and then the width of CBG obviously enlarges compared with the cylinder piles shown in Fig. 3(a). Third, for the hollow square pile structures, four CBGs appear in the periodic composite shown in Fig. 3(c). The first CBG (between 8.02Hz and 23.25Hz) with a width of 15.23Hz is produced between the sixth and seventh bands. The second CBG (between 23.40Hz and 24.10Hz) with a width of 0.47Hz is produced between the eighth and ninth bands. The third CBG (between 24.10Hz and 25.19Hz) with a width of 1.09Hz is produced between the ninth and tenth bands. The fourth CBG (between 25.19Hz and 27.02Hz) with a width of 1.83Hz is produced between the tenth and eleventh bands. It is worth noting that the second, third and fourth CBGs are merged into a CBG because the ninth and tenth bands are flat. In Fig. 3(c), it can be easily found that the lower band edge of the first CBG for the metamaterial with

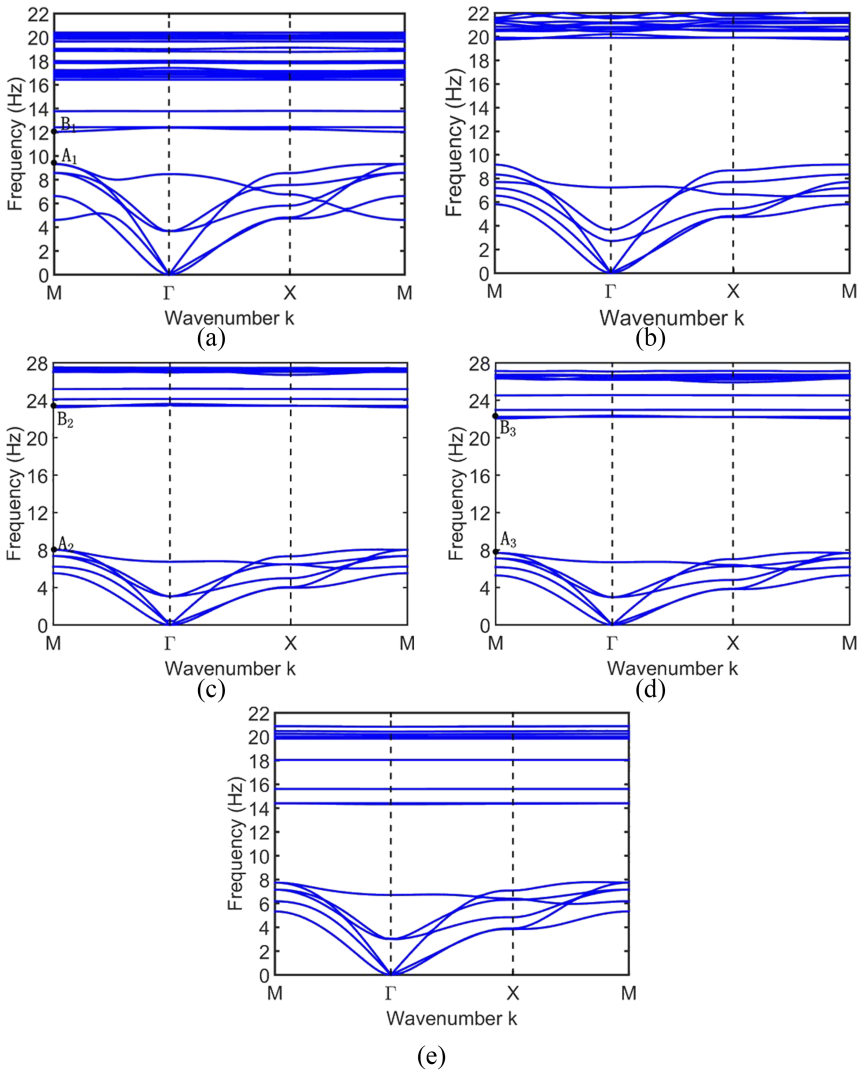

FIG. 3. Band structures with different structures for Lamb waves: (a) hollow cylinder, (b) hollow rectangle pile, (c) hollow square pile, (d) concrete-filled square pile, (e) soil-filled square pile.

a square cross-section decreases and upper band edge increases, compared with that of the circular cross-section (in Fig. 3(a)). Thus, the total width of 18.62Hz for a square cross-section is more than twice that of a circular cross-section (7.78Hz). It is also found that for hollow cylinder structure, more modes appear in the same frequency range, which results in a narrowing of the width of the CBGs. Moreover, the CBG width of square pile shown in Fig. 3(c) is larger than that of the rectangle pile (in Fig. 3(b)) by about 76%, and more importantly, it is isotropic to simplify the design of seismic shield. These comparative results imply the significant influence of the cross-sectional shape on the bandgap. Therefore, the metamaterial with a square cross-section seems favorable to open wider and lower frequency bandgaps which has practical potential applications.

Next, we study a square pile filled with a concrete inclusion, as shown in Fig. 1(d) and its corresponding band structure is illustrated in Fig. 3(d). The first CBG lies between the sixth and seventh bands for frequencies from 7.69Hz to 22.07Hz. The higher CBG extends from 23.23Hz to 26.34Hz between the eighth and eleventh bands due to the folding of the second, third and fourth CBGs. Furthermore, we find that the shape and position of the CBGs for concrete-filled piles are almost the same as those for non-filled structures (see Fig. 3(c) and (d)).

In addition, we replace concrete with soil in Fig. 1(d) and its corresponding band structure is shown in Fig. 3(e). The first CBG lies between the sixth and seventh bands for frequencies from

7.75Hz to 14.40Hz. The higher CBG caused by merging the second, third and fourth CBGs extends from 14.41Hz to 19.84Hz. Compared with the concrete-filled structure, it is shown that the lower band edge of the first CBG is at almost the same frequency, however, the upper band edge shifts down from 22.07Hz to 14.40Hz and the width decreases by about 7.67Hz, as shown in Fig. 3(e). It can also be found that the lower-order modes remain unchanged, while higher-order modes shift down with the decreasing of cut-off frequency. Therefore, the design solution using concrete-filled pile is proven to be preferable compared to the case of soil-filled pile for seismic applications.

B. Vibration modes for Lamb waves

To understand the formation mechanism of the bandgaps for Lamb waves, we calculate the vibration modes at the edges of the first complete bandgaps. The upper and lower band edges are marked as A_1 and B_1 for the hollow cylinder, A_2 and B_2 for the hollow square pile, and A_3 and B_3 for the concrete-filled square pile, respectively (see Fig. 3). The 3D and 2D views of vibration modes are shown in Fig. 4. It is noted that the square lattice of these resonant structures can be regarded as a periodic arrangement of the scatterers (steel part) connected by narrow connectors (soil part). For the lower band edge-modes, the scatterers oscillate as rigid bodies, and the connectors act as springs between the neighboring scatterers, as shown in Fig. 4(a), (c) and (e). For the upper band edge-modes, the connectors oscillate and the scatterers are nearly still, as shown in Fig. 4(b), (d) and (f). Fig. 4(a) and (b) correspond to the lower (A_1) and upper (B_1) edge modes of the first CBG for the

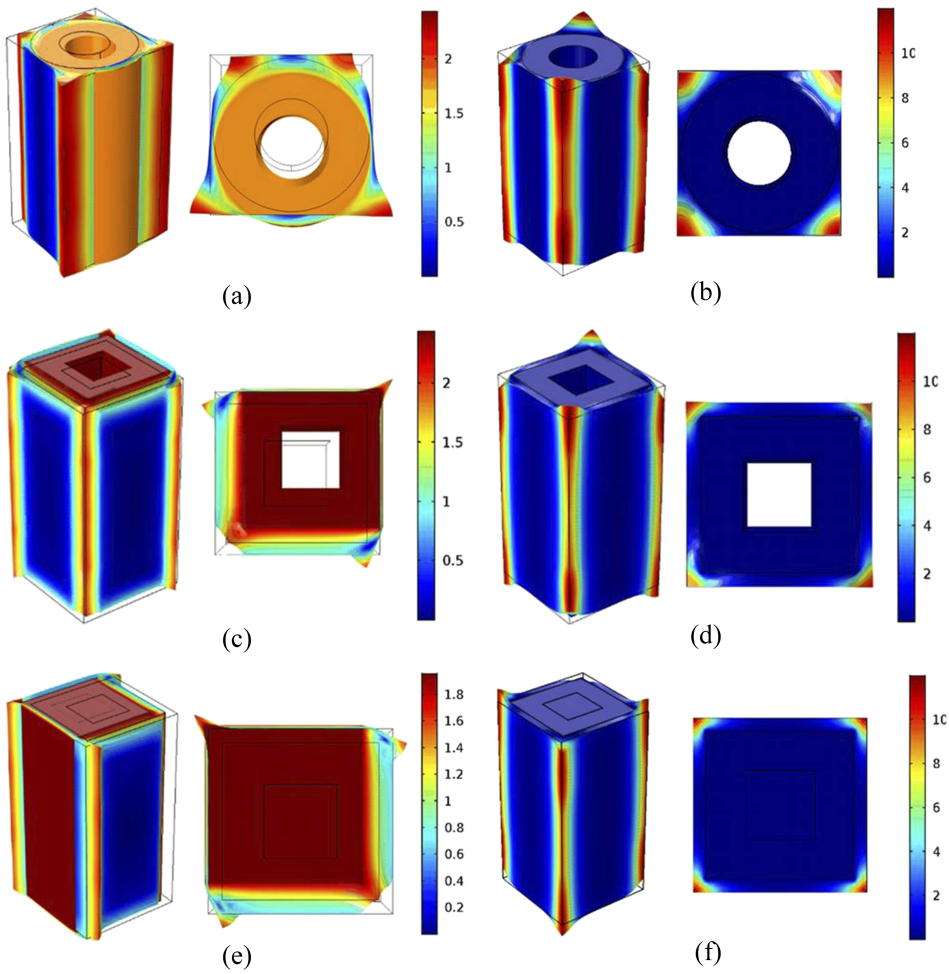

FIG. 4. Vibration modes at the edges of the first CBGs. Panels (a)and (b) correspond to point A_1 and B_1 for the hollow cylinder, (c) and (d) correspond to point A_2 and B_2 for the hollow square pile, and (e) and (f) correspond to point A_3 and B_3 for concrete-filled square pile.

hollow cylinder. The vibration of the scatterers is produced in the *y*-axis direction and homogeneously distributed in the thickness direction. Thus, this mode is independent of the thickness and also appears in the band structures of the bulk systems.[33] Coupling between scatterers and long traveling waves in the substrate contributes to the bandgap (see the total displacement deformation on *x*-*y* plane in Fig. 4(a)). However, at the point B_1 the connector vibrates in the *z*-direction and the scatterer hardly vibrates (see Fig. 4(b)). The vibrations are almost uniformly distributed in the thickness direction. Thus, this is the zeroth-order mode independent of the thickness. Figures 4(c) and (d) show the lower (A_2) and upper (B_2) edge modes of the first CBG for the hollow square pile. It is noted that vibration occurs in the two diagonal directions of unit cell and produces a resultant force of the *x*- and *y*-directions at the point A_2. The adjacent connectors in a unit cell vibrate distinctly around the scatterer in anti-phase, whereas the diagonal connectors vibrate in-phase. The mode at point B_2 is similar to that at point B_1. The scatterer keeps still and the connectors vibrate up and down. Figures 4(e) and (f) illustrate the vibration modes at the lower (A_3) and upper (B_3) edges of the first CBG for the concrete-filled pile. Obviously, the mode shapes for concrete-filled square pile are similar to those of the hollow square pile because the combination of the steel part and concrete inclusion is equivalent to a scatterer. This similarity is beneficial for practical application because the concrete-filled pile can be constructed under the foundation of a building and the hollow square pile can be constructed around a building for cost savings.

C. Effect of geometric parameters

From the analysis above, we can conclude that the generation of wide bandgaps in the system with a square cross-section is due to the local resonance of the resonant unit with large scatterer connected by narrow connectors. The structural parameters in a resonant unit play a fundamental role in the nucleation of the CBGs. In the following section, we will analyze the effect of a single parameter on the bandgap characteristics while other parameters are left unchanged. This study is performed for the metamaterial comprised of hollow square piles.

If the ration *b*/*a* varies, while the mechanical parameters and other geometric parameters remain the same as previously mentioned, the influence of the ratio *b*/*a* on the width of CBGs can be illustrated as shown in Fig. 5(a). In the figure, CBG widening and shifting towards higher frequencies as *b*/*a* increases is highlighted. Although the lower bound of the first CBG is almost unaltered, its width is enlarged due to the shift of the upper bound towards higher frequencies. In general, as *b*/*a* increases, the first CBG size evidently increases while the second CBG size increases initially, but remains stable beyond *b*/*a*=0.7.

The influence of the steel pile thickness *b*-*c* on the width of the CBGs is shown in Fig. 5(b). The first CBG widens slowly as the thickness increases, whereas the size of the second CBG decreases initially, but remains almost unaltered beyond $(b\text{-}c)/a = 0.25$. The optimal parameter is around 0.45. This analysis allows us to define optimal parameters for the hollow square pile cross-section.

Simulations show that the unit cell height influences inhibited frequencies smaller than other considered parameters shown in Fig. 5(c), at least for the first CBG. The lower bound of the first CBG is almost unaltered and the upper bound fluctuates slightly with the increase of *h*/*a*. It is worth noting that the size of the first CBG is preserved, while the second CBG size decreases. This can be explained by considering the mode shapes localized in the resonant units. Vibration patterns for higher order modes are characterized by localized motions within the substrate. As shown in Fig. 6, these mode shapes with a out-of-plane displacement correspond to the point $M = (\pi/a,\pi/a)$ for the eighth band at f=23.40Hz, the ninth band at f=24.10Hz and the tenth band at f=25.19Hz. The vibrations are distributed along the *z*-axis, so the height plays a significant role in the high frequency bandgaps. With the increase of height, the narrowing of the CBG is caused by the appearance of additional modes and will eventually close.[34] The total CBGs are the widest at *h*/*a*=2. In addition, optimal parameter values are indicated in Fig. 5 with dashed-dotted lines, considering both sufficient CBG properties and practical realization of the structure.

D. Effect of material parameters

Next, we consider the effect of the elastic parameters of soil on evolution of CBGs where the Young's modulus and density of soils typically vary in the range of 1-90MPa and 1600-2200kg/m^3,

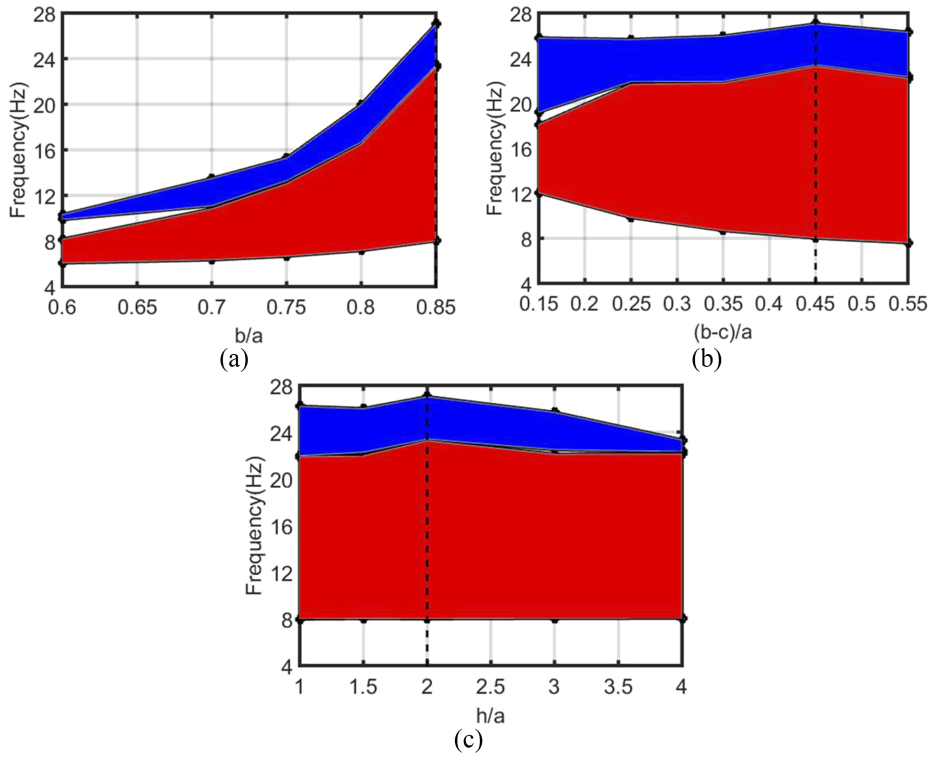

FIG. 5. The upper and lower frequency bounds of CBGs as a function of different geometric parameters for hollow square column: (a) the ratio of outer side length b to lattice constant a, (b) the ratio of steel thickness (b-c) to lattice constant a, (c) the ratio of height h to lattice constant a. The red shades represent the first CBGs and the blue shades represent the merged CBGs. Optimal parameter values are indicated with dashed lines.

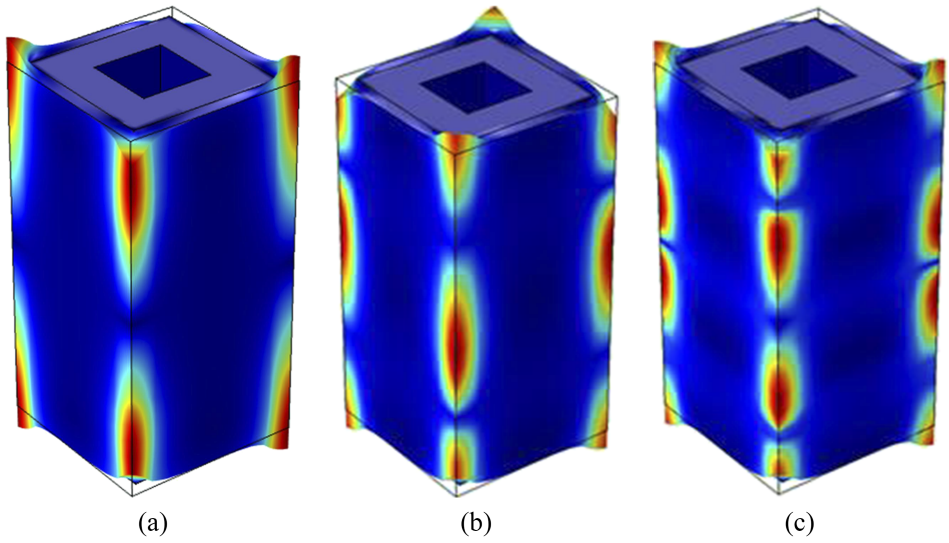

FIG. 6. Vibration modes for the hollow square column at point M of the different bands: (a) the eighth band at f=23.40Hz, (b) the ninth band at f=24.10Hz, (c) the tenth band at f=25.19Hz.

respectively. The Poisson's ratio and all geometric parameters are left unaltered, while the Young's modulus and material density are varied. Simulations show that when the modulus of the soil increases from 1MPa to 90MPa, the first CBG enlarges rapidly and shifts towards a higher frequency range,

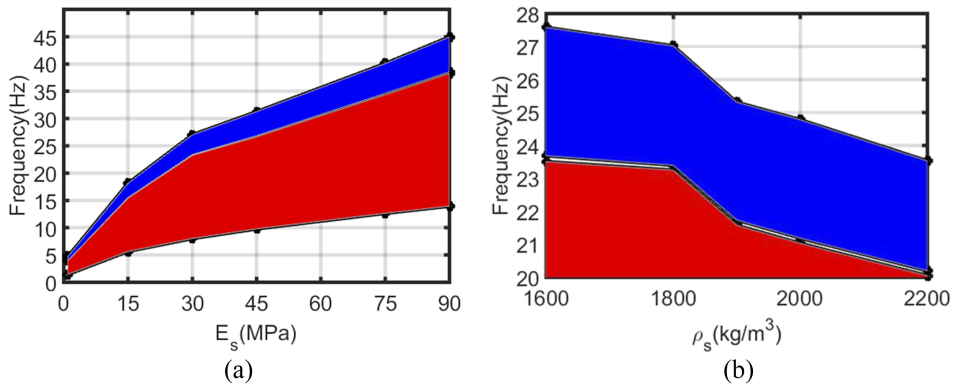

FIG. 7. Effect of different mechanical parameters of soil on CBGs: (a) the Young's modulus; (b) the mass density. The red shades represent the first CBG and the blue shades represent the second CBG.

and the second CBG has the same changing trend as the first CBG, as shown in Fig. 7(a). In contrast, when the density of the soil increases from 1600kg/m^3 to 2200kg/m^3, the first CBG starts with a broad width and then narrows sharply. It also steadily shifts to a lower frequency range before finally leading to its closure, as shown in Fig. 7(b). The second CBG shifts to a lower frequency range, while its width remains almost invariable. The evolution trend of these CBGs suggests that the Young's modulus and mass density of the soil have a significant impact on the location and width of CBGs. These results also indicate that we need to consider the mechanical parameters of soils at the different building sites to achieve desired CBGs.

E. Frequency domain analysis of periodic square piles

In this section, we take the soil-filled square pile model as an example to present the results of earthquake shielding based on FEM. The transmission coefficient of surface wave propagation is calculated to verify the simulated CBGs for Lamb waves, and the displacement fields in the periodic composite are observed to demonstrate the shielding capability of the proposed metamaterial. The other properties can be also observed in elastic wave propagation in the proposed metamaterial, such as the reflection, the refraction and the attenuation of Lamb waves.

We evaluate the transmission characteristics of a finite periodic composite system consisting of an array of soil-filled square piles sandwiched by two homogeneous parts of the soil. The frequency domain calculations are performed using COMSOL for a structure composed of 80 unit cells. The cells are arranged in a 2D array along the x- and y-directions. The parameters of the unit cell remain the same as the reference parameters mentioned above, as shown in Fig. 1(d). Perfectly matched layers are applied to the two ends along x-direction to absorb reflections from the domain boundaries. Periodic boundary conditions are applied to the finite periodic composite along y-direction. An incident surface wave with polarizations along x- and y-directions is applied at the interface between the perfectly matched layer and the homogeneous part on the left side of the model. The frequency domain analysis sweeping from 0Hz to 22Hz is performed and the transmission coefficient as a function of frequency along ΓX direction is calculated as shown in Fig. 8. The attenuation regions in Fig. 8 agree well with the bandgaps along the ΓX direction in the band structure of the periodic composite in Fig. 3(e).

To further validate the shielding capability of the proposed seismic metamaterial, we present the total displacement fields for the incident wave within and beyond the CBGs. The total displacement fields at frequencies of 3.4Hz and 10.2Hz are shown in Fig. 9. At 3.4Hz (see Fig. 9(a)) below the bandgap, the incident surface wave is partially reflected and partially passes through the periodic composite. In contrast, the incident wave is almost totally reflected and confined in the left homogeneous section when the incident wave frequency is 10.2Hz (see Fig. 9(b)) within the bandgap. This analysis shows that the vibration is efficiently attenuated for guided Lamb waves with frequency inside the CBG. Therefore, the seismic shield can provide a virtually unperturbed area, even if reflections at the free boundaries of the volume are included.

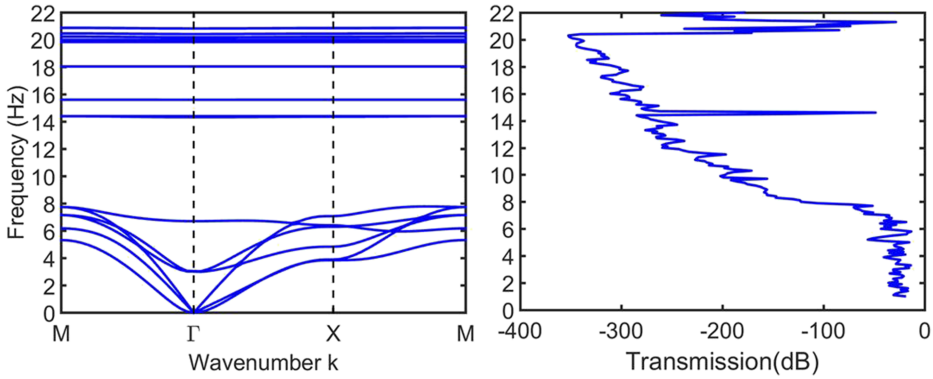

FIG. 8. The frequency domain analysis sweeping from 0Hz to 22Hz is performed and the transmission coefficient as a function of frequency.

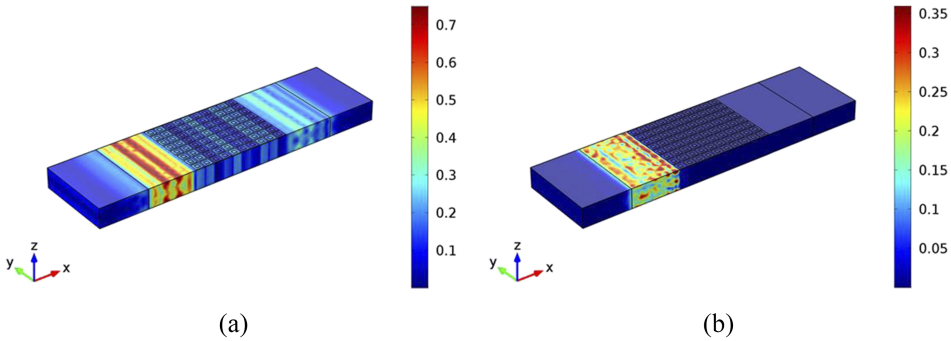

FIG. 9. The total displacement fields at different frequencies: (a) 3.4Hz and (b) 10.2Hz.

F. Band structures and vibration modes for surface waves

As we know, seismic waves carrying energy propagate through soft superficial alluvial layers from the focus. When they reach the surface, refraction or scattering phenomena occur on strong topographic irregularities and surface waves are generated that propagate along the Earth's surface, which can strongly increase the amplitude of the ground motion. The wavelengths range from a few meters to a few hundred meters corresponding to frequencies from less than 50Hz to a few Hertz. These lengths are similar to the sizes of buildings, which would lead to potential building resonance phenomena[16] in the case of earthquakes.

Here, we choose two structures (shown in Fig.'s 1(a) and (c)) from the previous structures applied for Lamb waves to investigate the performance of shielding surface waves, because our main focus is to check whether bandgaps exist for surface waves in a half space. The method describing surface waves is an equivalent method by adding a substrate with a thickness of 10a at the bottom of pile, as shown in Fig.'s 10(a) and (d). The z-axis is defined to be perpendicular to the substrate surface and parallel to the pile axis. A 3D mesh is used and the structure is assumed to be infinite and periodic in both the x- and y-directions. The computation of the band structures is performed as follows.[36–38] First, a finite system with a thickness larger than lattice period is computed in a unit cell with specific boundary conditions. The stress-free boundary conditions are applied to the top surfaces and fixed boundary conditions to the bottom surfaces. Periodic boundary conditions are applied to the interfaces between the adjacent cells according to Bloch-Floquet theorem. Then, a sound cone is introduced in the FIBZ to separate the radiative region and nonradiative region which contains only surface waves and is overlaid as a region on the band structures.

Next, the band structure and displacement field calculations are performed to investigate the propagation of surface waves for both types of unit cells shown in Fig. 10. For the unit cell with a hollow cylinder, the surface wave modes are localized inside the sound cone while the bulk wave

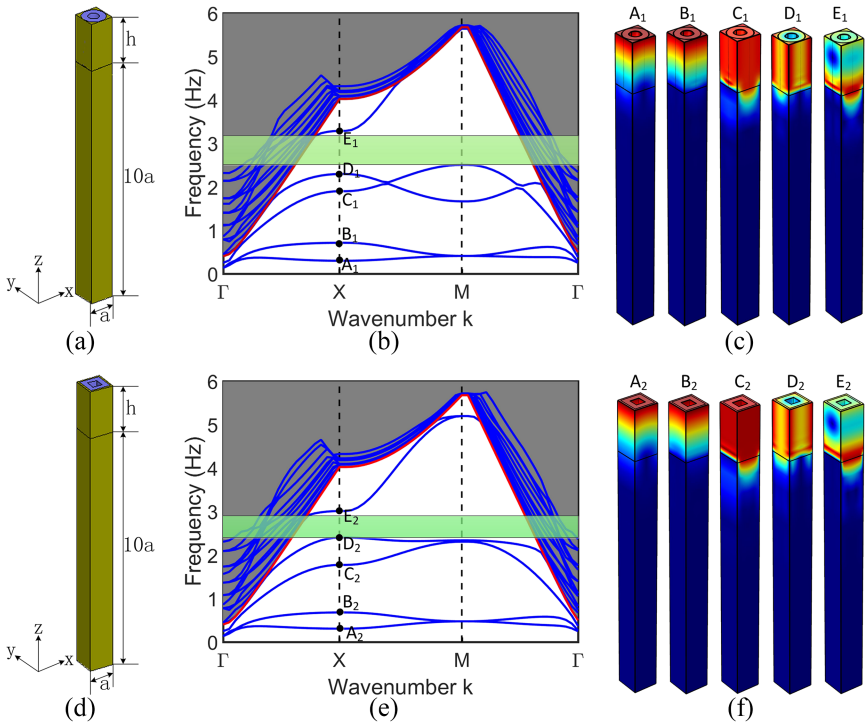

FIG. 10. Model and calculations for the hollow cylinder: (a) the unit cell used for band structure calculations with the square lattice constant a = 10m, the height of hollow cylinder $h = 2a$ and the height of substrate $10a$, (b) band structure along high symmetry directions of FIBZ for surface waves and (c) corresponding mode shapes at point A_1, B_1, C_1, D_1 and E_1. Model and calculations for the hollow square pile: (d) the unit cell used for band structure calculations with the square lattice constant a = 10m, the height of hollow square pile $h = 2a$ and the height of substrate $10a$, (e) band structure and (f) corresponding mode shapes at point A_2, B_2, C_2, D_2 and E_2. The gray region represents the sound cone of the soil substrate and green region represents the complete bandgap. The red line limiting the sound cone is given by the smallest phase velocity in the substrate.

modes are outside of it, as shown in Fig. 10(b). We can see that one complete band gap appears around 2.79Hz in the band structure. To elucidate the mechanism of the dispersion curves inside the sound cone, the displacement fields of some surface modes are obtained. Figure 10(c) shows the displacement fields of different guided surface modes and these modal shapes correspond to the points indicated in the band structures in Fig. 10(b). Here, the wave vector k_x is selected close to the X-point of the first Brillouin zone. We can see that polarizations of these guided modes are more complex than those of Rayleigh waves propagating on a homogenous surface because the Rayleigh wave becomes dispersive. The bands containing modes A_1, B_1, C_1, D_1 and E_1 correspond to guided surface modes with different penetration depths and polarizations. The modes at A_1 and C_1 have mostly in-plane polarization, and the modes at B_1, and D_1 have mostly sagittal polarization.[36] However, the mode at E_1 is too complex to describe its type. For the unit cell with a hollow square pile, the band structures in Fig. 10(e) and corresponding surface modes in Fig. 10(f) present similar behaviors to the unit cell with a hollow cylinder since they are similar structures. One complete band gap is obtained around 2.71Hz in the band structure. Note that the almost flat dispersion curves containing modes A_2, B_2 and D_2 correspond to localized resonant modes which are shown in Fig. 10(f). Hence, the dispersion modes of the considered metamaterial result from the interaction of these guided surface waves with the piles. Therefore, previously designed resonant structures for Lamb waves still have complete bandgaps in a half-space for surface waves.

IV. CONCLUSION

In this paper, we construct an elastic metamaterial with complete bandgaps to isolate a region around a protected building from seismic waves. For Lamb waves, the bandgap responses of various

basic resonant structures are analyzed to provide a comparison. We find that the periodic composite with a square cross-section is much more favorable for the formation of wide CBGs with a bandgap width of 18.62Hz around the frequency 15Hz. We calculate the vibration modes at the edges of the first CBGs to show the bandgap formation mechanism. The shape, height and material properties of the structure play a crucial role in the evolution of CBGs. Thus, we report the dependence of CBGs on the geometric parameters of piles and material properties of soil, in order to obtain the optimal parameters. The transmission coefficient of wave propagation and the behavior of vibrations are presented to show the efficiency of earthquake shielding. For surface waves, we have calculated the band structures with hollow cylinder and square pile by considering specific boundary conditions and the introduction of sound cone limitation. We have explored modal displacements to clearly demonstrate the nature of the bandgap for surface waves. This work demonstrates not only the promising potential applications as seismic shields but also provides design guidelines for civil engineers.

ACKNOWLEDGMENTS

National Natural Science Foundation of China under Grant No.41404041, China Postdoctoral Science Foundation under Grant No.2014M562079 and Special Financial Grant from China Postdoctoral Science Foundation No. 2016T90739 have supported this research.

[1] Z. Shi and J. Huang, Soil Dynamics and Earthquake Engineering **50**, 204–212 (2013).
[2] M. D. Symans, F. A. Charney, A. S. Whitaker, M. C. Constantinou, C. A. Kircher, M. W. Johnson, and R. J. McNamara, Journal of Structural Engineering **10**, 1061 (2008).
[3] D. R. Smith, W. J. Padilla, D. C. Vier, S. C. Nemat-Nasser, and S. Schultz, Phys. Rev. Lett. **84**, 4184–4187 (2000).
[4] W. X. Jiang, T. J. Cui, X. M. Yang, Q. Cheng, R. Liu, and D. R. Smith, Appl. Phys. Lett. **93**, 194102 (2008).
[5] Z. Liu, X. Zhang, Y. Y. Zhu, Z. Yang, C. T. Chan, and P. Sheng, Science **289**, 1734 (2000).
[6] N. Fang, D. J. Xi, J. Y. Xu, M. Ambrati, W. Sprituravanich, C. Sun, and X. Zhang, Nat. Mater. **5**, 452 (2006).
[7] R. V. Craster and S. Guenneau, *Acoustic Metamaterials: Negative Refraction, Imaging, Lensing and Cloaking* (Springer, Berlin, 2013).
[8] S. Benchabane, A. Khelif, J.-Y. Rauch, L. Robert, and V. Laude, Phys. Rev. E **73**, 065601 (2006).
[9] M. Brun, S. Guenneau, and A. B. Movchan, Appl. Phys. Lett. **94**, 061903 (2009).
[10] A. N. Norris and A. L. Shuvalov, "Elastic cloaking theory," Wave Motion **48**, 525 (2011).
[11] A. Sukhovich, B. Merheb, K. Muralidharan, J. O. Vasseur, Y. Pennec, P. A. Deymier, and J. H. Page, Phys. Rev. Lett. **102**, 154301 (2009).
[12] M. Farhat, S. Guenneau, and S. Enoch, Phys. Rev. Lett. **103**, 024301 (2009).
[13] M. Farhat, S. Guenneau, and S. Enoch, Phys. Rev. B **85**, 020301R (2012).
[14] M. Dubois, M. Farhat, E. Bossy, S. Enoch, S. Guenneau, and P. Sebbah, Appl. Phys. Lett. **103**, 071915 (2013).
[15] S. Brûlé, E. H. Javelaud, S. Enoch, and S. Guenneau, Phys. Rev. L **112**, 133901 (2014).
[16] Y. Achaouia, B. Ungureanua, S. Enocha, S. Brûléc, and S. Guenneau, Extreme Mechanics Letters **8**, 30–38 (2016).
[17] J. Huang and Z. Shi, International Journal of Geomechanics **13**, 132–142 (2013).
[18] Y. Xiao, J. Wen, and X. When, Journal of Physics D: Applied Physics **45**, 195401 (2012).
[19] A. Colombi, P. Roux, S. Guenneau, P. Gueguen, and R. V. Craster, Scientific Reports **6**, 19238 (2016).
[20] D. J. Colquitt, A. Colombi, R. V. Craster, P. Roux, and S. R. L. Guenneau, arXiv:1608.01792, 2016.
[21] C. Park, N. Ryden, R. Westerhoff, and R. Miller, *Proc.SEG Int. Symp. (Salt Lake City)* 2002.
[22] P. Bormann, B. Engdahland, and R. Kind, "Seismic wave propagation and earth models," *New Manual of Seismological Observatory Practice* (Potsdam: Deutsches Geo Forschungs Zentrum GFZ) pp 1–70, 2009.
[23] D. Torrent and J. S. Dehesa, New Journal of Physics **10**, 063015 (2008).
[24] D. P. Elford, L. Chalmers, F. V. Kusmartsev, and G. M. Swallowe, J. Acoust. Soc. Am. **130**, 2746–2755 (2011).
[25] X. Zhou, Y. Wang, and C. Zhang, J. Appl. Phys. **106**, 014903 (2009).
[26] T. Ma, Y. Wang, Y. Wang, and X. Su, Optics Express **21**, 2727–2732 (2013).
[27] Z. Z. Yan and Y. S. Wang, Phys. Rev. B **74**, 224303 (2006).
[28] N. Papanikolaou, I. E. Psarobas, and N. Stefanou, Appl. Phys. Lett. **96**, 231917 (2010).
[29] F. L. Li, Y. S. Wang, Ch. Zhang, and G. L. Yu, Wave Motion **50**, 525 (2013).
[30] A. Khelif, B. Aoubiza, S. Mohammadi, A. Adibi, and V. Laude, Physical Review E **74**, 046610 (2006).
[31] X. C. Wang, *Finite Element Method* (Tsinghua University Press, Beijing, 2003, in Chinese).
[32] Y. F. Wang, Y. S. Wang, and X. X. Su, Journal of Applied Physics **110**, 113520 (2011).
[33] Y. F. Wang and Y. S. Wang, Journal of Sound and Vibration **332**, 2019–2037 (2013).
[34] R. Zhu, G. L. Huang, H. H. Huang, and C. T. Sun, Physics Letters A **375**, 2863–2867 (2011).
[35] A. Khelif, Y. Achaoui, S. Benchabane, V. Laude, and B. Aoubiza, Physical Review B **81**, 214303 (2010).
[36] Y. Achaoui, A. Khelif, S. Benchabane, L. Robert, and V. Laude, Physical Review B **83**, 104201 (2011).
[37] M. B. Assouar and M. Oudich, Applied Physics Letters **99**, 123505 (2011).
[38] Y. Li, Z. L. Hou, M. Oudich, and M. B. Assouar, Journal of Applied Physics **112**, 023524 (2012).
[39] B. Graczykowski, F. Alzina, J. Gomis-Bresco, and C. M. Sotomayor Torres, Journal of Applied Physics **119**, 025308 (2016).
[40] T. W. Liu, Y. C. Tsai, Y. C. Lin, T. Ono, S. Tanaka, and T. T. Wu, AIP Advances **4**, 124201 (2014).